Multi-source land-use emissions reveal rising airborne fraction

J. Eduardo Vera-Valdes

2026-05-23

The airborne fraction is the share of human carbon dioxide emissions that remains in the atmosphere, and it is a key indicator of how the climate system is responding to continued emissions[1,2]. Whether this share is rising remains debated because conclusions depend strongly on uncertain estimates of emissions from land-use and land-cover change (LULC). To address this, we use all available LULC measurement series constructed from Global Carbon Budget 2025 data[3] and apply a trend framework that explicitly accounts for measurement uncertainty[4–6]. We show that the airborne fraction has increased over time, and that this conclusion remains when we test sensitivity to excluding the final year and to serial dependence in annual data[7]. These results strengthen evidence that a growing share of emitted carbon dioxide is accumulating in the atmosphere rather than being taken up by land and ocean sinks, with direct implications for carbon-budget assessments and near-term mitigation requirements.

Background

Whether the airborne fraction (AF) is increasing or approximately constant remains contested[1,2,8–12]. In its classical form, AF is a yearly ratio of atmospheric growth to total anthropogenic emissions, computed as the sum of fossil fuel emissions and land-use and land-cover change emissions:

$$AF_t = \frac{G_t}{FF_t + LULC_t}, \tag{1}$$

where G_t is the annual atmospheric CO_2 growth, FF_t is fossil fuel emissions excluding carbonation, and $LULC_t$ is land-use and land-cover change emissions. AF is a key carbon-cycle diagnostic, with implications for carbon-cycle feedbacks and near-term mitigation planning[1–3].

A persistent concern is that AF inference depends on the treatment of land-use and land-cover change (LULC) emissions, which are uncertain and model-dependent in annual carbon-budget accounting[3]. The Global Carbon Budget (GCB) 2025 dataset provides one column of LULC emissions as the average of three bookkeeping models (BLUE, OSCAR, LUCE), but a broader set of model-based LULC alternatives can be constructed from the same source data. If the information from this broader set of LULC measurements is not incorporated into AF trend inference, tests can be underpowered and inference on trend direction becomes less reliable.

Here we address that issue with a design that incorporates measurement uncertainty to obtain more reliable trend estimates[4–6]. We present a two-stage estimator that propagates denominator uncertainty from repeated LULC measurements into annual AF variance and then estimates the AF trend by weighted least squares (WLS) with heteroskedasticity- and autocorrelation-consistent (HAC) inference[7]. The approach uses cross-measurement dispersion to weight years by precision, rather than treating all years as equally precise as in ordinary least squares (OLS). We find that WLS delivers statistically significant and more stable evidence of positive trend, including under exclusion of the final observation (2024), which shows a large AF jump. For comparison, we estimate OLS on the same AF series, with conventional and HAC standard errors showing weaker evidence of a positive trend and greater sensitivity to endpoint exclusion. This clarifies why evidence based on OLS does not support a clear conclusion about AF trends.

Data

We use annual Global Carbon Budget 2025 data for 1959-2024, with atmospheric growth G_t from NOAA/ESRL global concentration trends[13], fossil emissions excluding carbonation FF_t from the Global Carbon Project fossil dataset[3], and a panel of 69 LULC measurements per year: BLUE[14], OSCAR[15], LUCE[16], and peat-augmented process-based land-model combinations drawn from the GCB model ensemble[17–37], combined with peat components[38–40] (see Methods). The data is shown in Figure 1.

Two LULC means are constructed from the panel. First, the GCB LULC mean, defined as the mean of the three bookkeeping models BLUE, OSCAR, and LUCE, corresponds to the LULC column used in the Global Carbon Budget. Second, the all-LULC mean, defined as the cross-series mean from all 69 LULC measurements. Uncertainty from the

multiple LULC measurements are estimated by the cross-measurement dispersion from the full panel.

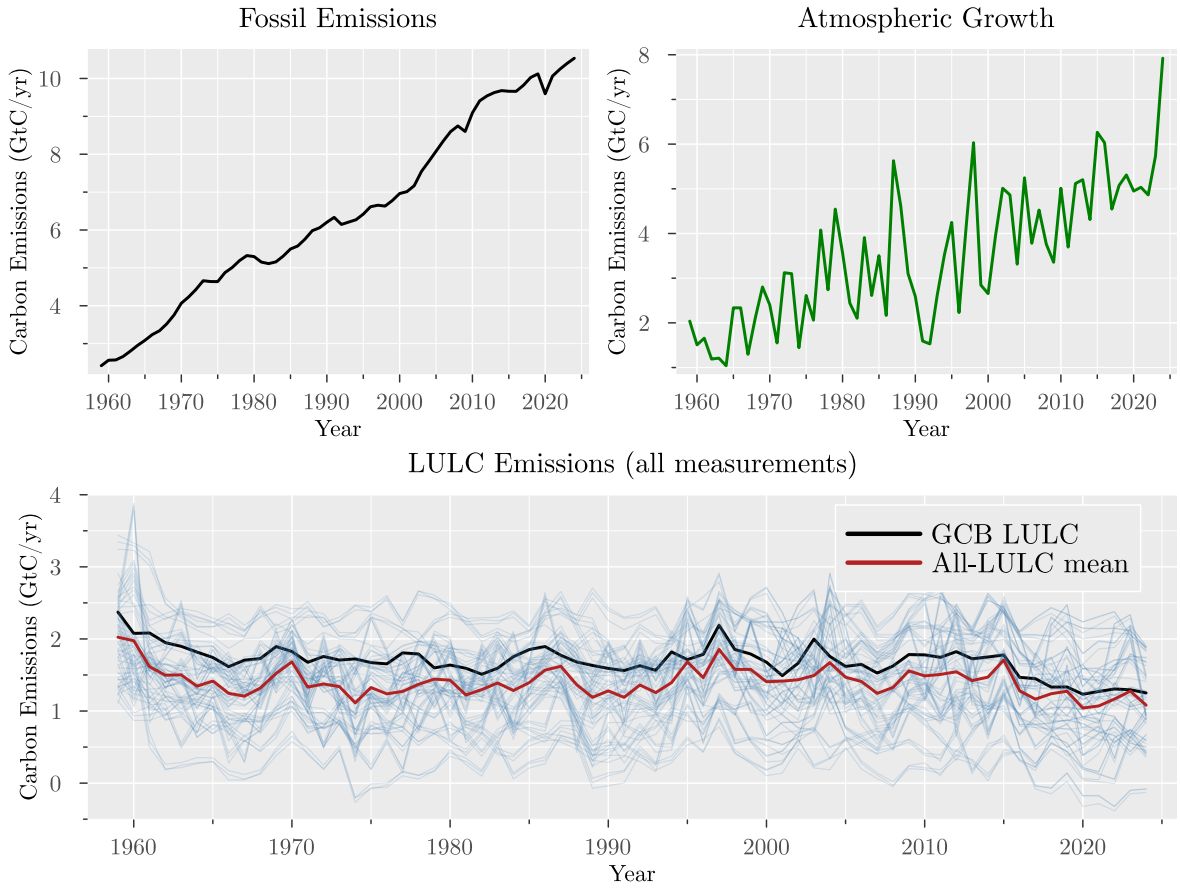

Figure 1: Global Carbon Budget 2025 data for fossil emissions, atmospheric growth, and LULC emissions (1959-2024). For the LULC panel, we show all extracted and derived LULC measurements together with the GCB LULC column and the all-LULC cross-series mean.

Identification Strategy

The empirical question is whether AF has a positive linear trend. The key design choice is how to handle annual denominator uncertainty from multiple LULC measurements. OLS assigns equal precision to all years and therefore discards information from cross-measurement dispersion. Our preferred specification uses delta-method variance estimates[41,42] to construct year-specific weights and then estimates the trend by WLS, with HAC standard errors for inference[7,43] (see Methods).

Results

Full-sample trends

Table 1 reports full-sample trend estimates for the four specifications: OLS using GCB LULC, OLS using the all-LULC mean, WLS using the GCB LULC with all-LULC weights, and WLS using the all-LULC mean with all-LULC weights.

Table 1: Full-sample trend comparison across OLS and WLS specifications.

Trend, full sample	OLS (GCB)	OLS (all)	WLS (GCB)	WLS (all)
Estimate	0.001581	0.001172	0.002649	0.002305
Standard error	0.000771	0.000792	0.000022	0.000023
HAC standard error	0.000621	0.000643	0.000657	0.000672
p-value	0.040212	0.138912	0.000000	0.000000
HAC p-value	0.010837	0.068425	0.000056	0.000609
R-squared	0.061706	0.033086	0.148987	0.111070

The main finding is that incorporating denominator-measurement information via WLS substantially changes inference relative to both OLS benchmarks. In the full sample, all approaches produce a positive slope, and both WLS specifications provide much stronger evidence than OLS (HAC p-values 0.000056 and 0.000609 versus 0.010837 and 0.068425). The estimated WLS trend is also steeper (0.002305 per year versus 0.001581 and 0.001172), consistent with greater weight on years with lower denominator uncertainty. The WLS slope implies an increase of about +0.15 in AF over 1959-2024, compared with about +0.10 and +0.08 from the two OLS specifications. The R-squared is also higher for WLS, indicating a better fit when accounting for measurement uncertainty. Nevertheless, the R-squared values are small in absolute terms, signaling that AF is a noisy variable and that the trend is only one component of its variation.

Figure 2 shows the AF series using the mean of all LULC measurements together with the associated variance, the OLS trend, and the delta-method WLS trend when using the full sample. The gray bars show the relative weights (standardised so that the maximum weight is 1) assigned to each year in the WLS estimation, which are inversely proportional to the estimated variance of the AF estimate for that year.

Note that the WLS trends are steeper than the OLS trends, which is consistent with the numerical results in Table 1. The WLS specifications assign more weight to the more precisely measured years (e.g., 2000-2020 as shown by the width of the shaded area) and less weight to noisier years (e.g., 1960s-1970s), which helps reveal the positive trend signal in the data.

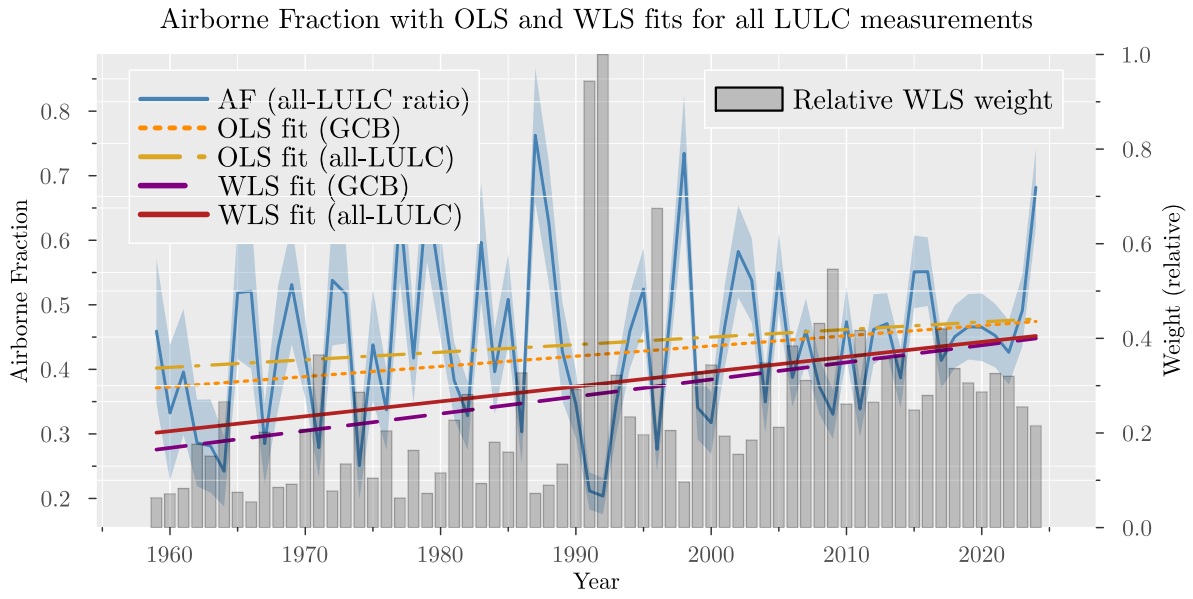

Figure 2: AF series with OLS and delta-method WLS trend (full sample, 1959-2024). Grey bars show the relative weights assigned to each year in the WLS estimation.

Endpoint Robustness

The final observation (2024) shows a large increase in AF. To ensure this point is not mechanically driving the result, we re-estimate the same four specifications on the subsample ending in 2023. Results are shown in Table 2 and Figure 3.

Table 2: Subsample (ending in 2023) trend comparison across OLS and WLS specifications.

Trend (up to 2023)	OLS (GCB)	OLS (all)	WLS (GCB)	WLS (all)
Estimate	0.001296	0.000878	0.002367	0.002015
Standard error	0.000777	0.000798	0.000022	0.000023
HAC standard error	0.000578	0.000600	0.000600	0.000615
p-value	0.095163	0.271089	0.000000	0.000000
HAC p-value	0.024954	0.143217	0.000081	0.001059
R-squared	0.042332	0.018863	0.125521	0.089297

Results remain qualitatively unchanged for the WLS specifications: both estimated slopes stay positive and statistically significant (0.002367 with HAC p-value = 0.000081, and 0.002015 with HAC p-value = 0.001059). For the sample ending in 2023, OLS using

GCB LULC is positive but only marginal under conventional inference (p-value = 0.095), while OLS using the all-LULC mean is not significant (p-value = 0.271). Overall, the WLS results are robust to endpoint exclusion, while OLS results are more sensitive to denominator construction and provide weaker evidence of a positive trend.

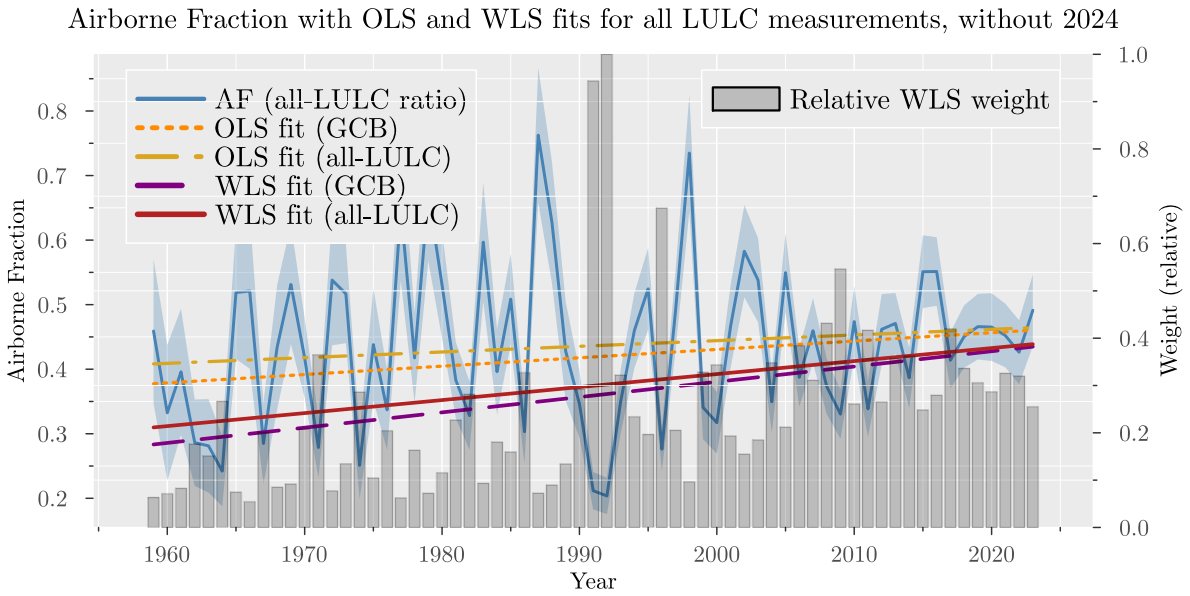

Figure 3: AF series with OLS and delta-method WLS trend (sample ending in 2023). Grey bars show the relative weights assigned to each year in the WLS estimation.

Supplementary Numerical Results

While the main focus is on the slope estimates, we also report intercept estimates for completeness. The intercept captures the baseline AF level in 1959, and its estimation can also be affected by denominator measurement error.

Results for the intercept estimates are shown in Table 3.

Table 3: Intercept comparison across OLS and WLS specifications for full sample and sample up to 2023.

Intercept	OLS (GCB) full	OLS (all) full	WLS (GCB) full	WLS (all) full	OLS (GCB) 2023	OLS (all) 2023	WLS (GCB) 2023	WLS (all) 2023
Estimate	−2.7266	−1.8946	−4.9141	−4.2130	−2.1611	−1.3121	−4.3539	−3.6377
Standard error	1.5352	1.5777	0.0443	0.0456	1.5461	1.5888	0.0440	0.0453

Intercept	OLS (GCB) full	OLS (all) full	WLS (GCB) full	WLS (all) full	OLS (GCB) 2023	OLS (all) 2023	WLS (GCB) 2023	WLS (all) 2023
HAC standard error	1.2391	1.2845	1.3212	1.3518	1.1553	1.1994	1.2087	1.2390
p-value	0.0757	0.2298	0.0000	0.0000	0.1622	0.4089	0.0000	0.0000
HAC p-value	0.0278	0.1402	0.0002	0.0018	0.0614	0.2739	0.0003	0.0033
R-squared	0.0617	0.0331	0.1490	0.1111	0.0423	0.0189	0.1255	0.0893

Discussion and conclusion

Using a measurement-error-aware framework, we find robust evidence that AF increased from 1959 to 2024. The key methodological point is that incorporating multi-source denominator uncertainty through delta-method WLS materially changes inference relative to plain OLS. The endpoint test shows that this conclusion is not driven by the 2024 jump.

In practice, the implication is clear: AF trend assessments should report measurement-error-aware weighted estimates, benchmark them against OLS, and document endpoint sensitivity.

A rising AF implies that a larger share of emitted CO_2 remains in the atmosphere over policy-relevant horizons, tightening near-term mitigation requirements for a given temperature objective[1–3]. The evidence of an increasing AF is consistent with broader findings that the climate system is out of energy balance and has recently exhibited elevated warming and heating rates; these results should therefore be interpreted within that wider risk context[44–47].

1. Canadell, J. G. *et al.* Contributions to accelerating atmospheric CO_2 growth from economic activity, carbon intensity, and efficiency of natural sinks. *Proceedings of the National Academy of Sciences* **104**, 18866–18870 (2007).
2. Raupach, M. R. *et al.* Global and regional drivers of accelerating CO_2 emissions. *Proceedings of the National Academy of Sciences* **104**, 10288–10293 (2007).
3. Friedlingstein, P. *et al.* Global carbon budget 2025. *Earth System Science Data* **18**, 3211–3288 (2026).
4. Fuller, W. A. *Measurement Error Models.* (Wiley, New York, 1987).
5. Carroll, R. J., Ruppert, D., Stefanski, L. A. & Crainiceanu, C. M. *Measurement Error in Nonlinear Models: A Modern Perspective.* (Chapman & Hall/CRC, Boca Raton, 2006).

6. Vera-Valdés, J. E. & Grivas, C. Robust estimation of carbon dioxide airborne fraction under measurement errors. *Environmental Research Communications* **7**, 031009 (2025).
7. Newey, W. K. & West, K. D. A simple, positive semi-definite, heteroskedasticity and autocorrelation consistent covariance matrix. *Econometrica* **55**, 703–708 (1987).
8. Knorr, W. Is the airborne fraction of anthropogenic CO_2 emissions increasing? *Geophysical Research Letters* **36**, L21710 (2009).
9. Ballantyne, A. P., Alden, C. B., Miller, J. B., Tans, P. P. & White, J. W. C. Increase in observed net carbon dioxide uptake by land and oceans during the past 50 years. *Nature* **488**, 70–72 (2012).
10. Le Quéré, C. *et al.* Trends in the sources and sinks of carbon dioxide. *Nature Geoscience* **2**, 831–836 (2009).
11. Bennedsen, M., Hillebrand, E. & Koopman, S. J. On the evidence of a trend in the CO2 airborne fraction. *Nature* **616**, E1–E3 (2023).
12. Bennedsen, M., Hillebrand, E. & Koopman, S. J. A regression-based approach to the CO2 airborne fraction. *Nature Communications* **15**, 8507 (2024).
13. Lan, X., Tans, P. & Thoning, K. W. Trends in globally-averaged CO2 determined from NOAA global monitoring laboratory measurements. (2026) doi:10.15138/9N0H-ZH07.
14. Hansis, E., Davis, S. J. & Pongratz, J. Relevance of methodological choices for accounting of land use change carbon fluxes. *Global Biogeochemical Cycles* **29**, 1230–1246 (2015).
15. Gasser, T. *et al.* Historical CO2 emissions from land use and land cover change and their uncertainty. *Biogeosciences* **17**, 4075–4101 (2020).
16. Qin, Z. *et al.* Global spatially explicit carbon emissions from land-use change over the past six decades (1961-2020). *One Earth* **7**, 835–847 (2024).
17. Haverd, V. *et al.* A new version of the CABLE land surface model (subversion revision r4601) incorporating land use and land cover change, woody vegetation demography, and a novel optimisation-based approach to plant coordination of photosynthesis. *Geoscientific Model Development* **11**, 2995–3026 (2018).
18. Melton, J. R. *et al.* CLASSIC v1.0: The open-source community successor to the canadian land surface scheme (CLASS) and the canadian terrestrial ecosystem model (CTEM) – part 1: Model framework and site-level performance. *Geoscientific Model Development* **13**, 2825–2850 (2020).
19. Lawrence, D. M. *et al.* The community land model version 5: Description of new features, benchmarking, and impact of forcing uncertainty. *Journal of Advances in Modeling Earth Systems* **11**, 4245–4287 (2019).

20. Fisher, R. A. *et al.* Taking off the training wheels: The properties of a dynamic vegetation model without climate envelopes, CLM4.5(ED). *Geoscientific Model Development* **8**, 3593–3619 (2015).
21. Tian, H. *et al.* North american terrestrial CO2 uptake largely offset by CH4 and N2O emissions: Toward a full accounting of the greenhouse gas budget. *Climatic Change* **129**, 423–426 (2015).
22. Ma, L. *et al.* Global evaluation of the ecosystem demography model (ED v3.0). *Geoscientific Model Development* **15**, 1971–1994 (2022).
23. Yang, X., Thornton, P., Ricciuto, D., Wang, Y. & Hoffman, F. Global evaluation of terrestrial biogeochemistry in the energy exascale earth system model (E3SM) and the role of the phosphorus cycle in the historical terrestrial carbon balance. *Biogeosciences* **20**, 2813–2836 (2023).
24. Needham, J. *et al.* Vertical canopy gradients of respiration drive plant carbon budgets and leaf area index. *New Phytologist* **246**, 144–157 (2025).
25. Felzer, B. S. & Jiang, M. Effect of land use and land cover change in context of growth enhancements in the united states since 1700: Net source or sink? *Journal of Geophysical Research: Biogeosciences* **123**, 3439–3457 (2018).
26. Xia, J. Z. *et al.* The carbon budget of china: 1980–2021. *Science Bulletin* **69**, 114–124 (2024).
27. Yue, X. *et al.* Development and evaluation of the interactive model for air pollution and land ecosystems (iMAPLE) version 1.0. *Geoscientific Model Development* **17**, 4621–4642 (2024).
28. Shu, S., Jain, A. K., Koven, C. D. & Mishra, U. Estimation of permafrost SOC stock and turnover time using a land surface model with vertical heterogeneity of permafrost soils. *Global Biogeochemical Cycles* **34**, e2020GB006585 (2020).
29. Reick, C. H. *et al.* JSBACH 3 - the land component of the MPI earth system model: Documentation of version 3.2. (2021) doi:10.17617/2.3279802.
30. Poulter, B., Frank, D. C., Hodson, E. L. & Zimmermann, N. E. Impacts of land cover and climate data selection on understanding terrestrial carbon dynamics and the CO2 airborne fraction. *Biogeosciences* **8**, 2027–2036 (2011).
31. Smith, B. *et al.* Implications of incorporating n cycling and n limitations on primary production in an individual-based dynamic vegetation model. *Biogeosciences* **11**, 2027–2054 (2014).
32. Schaphoff, S. *et al.* LPJmL4 – a dynamic global vegetation model with managed land – part 1: Model description. *Geoscientific Model Development* **11**, 1343–1375 (2018).
33. Lienert, S. & Joos, F. A bayesian ensemble data assimilation to constrain model parameters and land-use carbon emissions. *Biogeosciences* **15**, 2909–2930 (2018).

34. Vuichard, N. *et al.* Accounting for carbon and nitrogen interactions in the global terrestrial ecosystem model ORCHIDEE (trunk version, rev 4999): Multi-scale evaluation of gross primary production. *Geoscientific Model Development* **12**, 4751–4779 (2019).
35. Walker, A. P. *et al.* The impact of alternative trait-scaling hypotheses for the maximum photosynthetic carboxylation rate (v-cmax) on global gross primary production. *New Phytologist* **215**, 1370–1386 (2017).
36. Kato, E., Kinoshita, T., Ito, A., Kawamiya, M. & Yamagata, Y. Evaluation of spatially explicit emission scenario of land-use change and biomass burning using a process-based biogeochemical model. *Journal of Land Use Science* **8**, 104–122 (2013).
37. Ito, A. Disequilibrium of terrestrial ecosystem CO2 budget caused by disturbance-induced emissions and non-CO2 carbon export flows: A global model assessment. *Earth System Dynamics* **10**, 685–709 (2019).
38. Conchedda, G. & Tubiello, F. N. Drainage of organic soils and GHG emissions: Validation with country data. *Earth System Science Data* **12**, 3113–3137 (2020).
39. Müller, J. & Joos, F. Committed and projected future changes in global peatlands – continued transient model simulations since the last glacial maximum. *Biogeosciences* **18**, 3657–3687 (2021).
40. Qiu, C. *et al.* Large historical carbon emissions from cultivated northern peatlands. *Science Advances* **7**, eabf1332 (2021).
41. Cochran, W. G. *Sampling Techniques*. (Wiley, New York, 1977).
42. Oehlert, G. W. A note on the delta method. *The American Statistician* **46**, 27–29 (1992).
43. Aitken, A. C. On least squares and linear combination of observations. *Proceedings of the Royal Society of Edinburgh* **55**, 42–48 (1935).
44. Minière, A., Schuckmann, K. von, Sallée, J.-B. & Vogt, L. Robust acceleration of earth system heating observed over the past six decades. *Scientific Reports* **13**, 22975 (2023).
45. World Meteorological Organization. State of the global climate 2025. (2026) doi:10.59327/WMO/S/CRI/SOC/1.
46. Storto, A. & Yang, C. Acceleration of the ocean warming from 1961 to 2022 unveiled by large-ensemble reanalyses. *Nature Communications* **15**, 545 (2024).
47. Foster, G. & Rahmstorf, S. Global warming has accelerated significantly. *Geophysical Research Letters* **53**, e2025GL118804 (2026).

Methods

Our primary estimator is a two-stage measurement-error trend model using repeated yearly denominator measurements, followed by weighted trend estimation with HAC inference[4,5,7,42,43].

Construction of the LULC measurement panel

The repeated LULC measurements are built from the Global Carbon Budget 2025 dataset. We first extract the three bookkeeping series (BLUE, OSCAR, LUCE)[14–16]. Then, for each process-based land-model LULC model in the GCB ensemble which does not already include peat emissions[17–37], we add the corresponding peat component to make it comparable to the bookkeeping models, which include peat emissions by construction. Specifically, for each of the 33 process-based land-model combinations in the GCB ensemble we create three peat-augmented variants by adding FAO_peat, LPX_Bern_peat, and ORCHIDEE_peat[38–40]. This produces 66 derived series, and together with BLUE/OSCAR/LUCE gives a panel of 69 yearly LULC measurements.

In the estimation, the yearly denominator is computed as

$$\hat{C}_t = FF_t + \bar{LULC}_t, \qquad \bar{LULC}_t = \frac{1}{n_t}\sum_{j=1}^{n_t} LULC_{tj},$$

where $n_t = 3$ for the GCB LULC mean and $n_t = 69$ for the all-LULC mean. The variance of $\hat{C}_t$ is estimated from the cross-measurement dispersion across the 69 LULC values and is used to construct the year-specific AF variance estimate used for WLS weighting.

Assume for each time $t = 1, \ldots, T$ we observe:

- a single numerator b_t (e.g., atmospheric CO_2 growth), and
- multiple denominator measurements $c_{t1}, \ldots, c_{tn_t}$ with $n_t \geq 2$, which are noisy observations of a latent C_t.

Using the repeated denominator measurements, we can estimate the variance of the ratio estimator $a_t = b_t/C_t$ via the delta method, which accounts for the variability in C_t due to measurement error. The procedure is described in detail next.

Two-step estimation approach

We use a two-step approach to estimate the trend in the ratio $a_t = b_t/C_t$ over time, accounting for denominator measurement error.

Step 1: Estimate C_t and a_t

1. Estimate the "true" denominator at time t as the sample mean across available LULC measurements:
$$\hat{C}_t = \frac{1}{n_t} \sum_{j=1}^{n_t} c_{tj}.$$

We consider two variants of this denominator estimate: one using the GCB LULC column (the mean of BLUE, OSCAR, LUCE) and one using the all-LULC mean (the mean across all 69 LULC measurements).

The variance of $\hat{C}_t$ can be estimated from the multiple measurements.

With $n_t \geq 2$, an empirical estimator is

$$\widehat{\mathrm{Var}}(\hat{C}_t) = s_{c,t}^2, \qquad s_{c,t}^2 = \frac{1}{n_t - 1} \sum_{j=1}^{n_t} (c_{tj} - \bar{c}_t)^2, \qquad \bar{c}_t = \hat{C}_t.$$

2. Form the ratio estimate
$$\hat{a}_t = b_t/\hat{C}_t.$$

3. Use the multivariate delta method (shown below) to get an approximate variance of $\hat{a}_t$

$$\widehat{\mathrm{Var}}(\hat{a}_t) \approx \left(\frac{b_t}{\hat{C}_t^2}\right)^2 \widehat{\mathrm{Var}}(\hat{C}_t).$$

Step 2: WLS regression of $\hat{a}_t$ on time

For each time t, we obtain a point estimate $\hat{a}_t$ and an estimated variance $\widehat{\mathrm{Var}}(\hat{a}_t)$ that reflects the cross-measurement dispersion. We use these estimates to fit a linear trend via weighted least squares (WLS):

$$\hat{a}_t = \alpha + \beta t + \varepsilon_t, \quad \varepsilon_t \sim (0, \sigma_t^2), \quad \sigma_t^2 = \widehat{\mathrm{Var}}(\hat{a}_t).$$

In our application, the time index t is the year, and $\hat{a}_t$ is the estimated AF for that year. The variance σ_t^2 captures the standard error variance and the uncertainty in the AF estimate due to denominator measurement error, which varies across years depending on the number and variability of the LULC measurements. We use this variance to weight the regression, giving more weight to years with more precise AF estimates.

Assuming negligible correlation in ε_t across time, this is WLS with weights $w_t = \frac{1}{\sigma_t^2}$. If we suspect serial correlation, we can use HAC standard errors for inference on β without changing the point estimate. In practice, we use a HAC covariance estimator with a Bartlett kernel and Andrews automatic bandwidth selection[7]. In the results, we report both conventional and HAC standard errors.

Testing for a time trend is then a test of $\beta = 0$ versus $\beta \neq 0$ in this linear model, and using WLS we have used all the information in the repeated $\hat{a}_t$'s through the delta-method approximation.

Delta method for ratio variance estimation

Step-by-step derivation (first-order delta method):

Define the random vector and the function of interest as

$$X_t = \begin{bmatrix} b_t \\ \hat{C}_t \end{bmatrix}, \qquad g(X_t) = \frac{b_t}{\hat{C}_t}.$$

and let

$$\sigma_{b,t}^2 = \mathrm{Var}(b_t), \qquad \sigma_{C,t}^2 = \mathrm{Var}(\hat{C}_t), \qquad \sigma_{bC,t} = \mathrm{Cov}(b_t, \hat{C}_t).$$

1. Linearize g around the mean vector $(\mu_{b,t}, \mu_{C,t}) = \mathbb{E}[(b_t, \hat{C}_t)]$:

$$g(X_t) \approx g(\mu_{b,t}, \mu_{C,t}) + \nabla g(\mu_{b,t}, \mu_{C,t})^\top (X_t - \mathbb{E}[X_t]).$$

2. Compute the gradient:

$$\nabla g(b, C) = \begin{bmatrix} \partial g/\partial b \\ \partial g/\partial C \end{bmatrix} = \begin{bmatrix} 1/C \\ -b/C^2 \end{bmatrix}.$$

3. Write the covariance matrix of $(b_t, \hat{C}_t)$:

$$\Sigma_t = \begin{bmatrix} \sigma_{b,t}^2 & \sigma_{bC,t} \\ \sigma_{bC,t} & \sigma_{C,t}^2 \end{bmatrix}.$$

4. Apply the delta-method variance formula

$$\mathrm{Var}(g(X_t)) \approx \nabla g(\mu_{b,t}, \mu_{C,t})^\top \Sigma_t \nabla g(\mu_{b,t}, \mu_{C,t}),$$

and with plug-in evaluation at (b_t, C_t), this becomes

$$\mathrm{Var}(\hat{a}_t) \approx \left(\frac{1}{C_t}\right)^2 \sigma_{b,t}^2 + \left(\frac{b_t}{C_t^2}\right)^2 \sigma_{C,t}^2 - 2\frac{b_t}{C_t^3}\sigma_{bC,t}.$$

In practice, we use plug-in estimates (replace unknown moments by their empirical counterparts). This is the standard delta-method approximation for the variance of a ratio estimator.

5. In the case analysed in this paper, we have a single numerator measurement from a robust source per time, so we treat $\sigma_{b,t}^2$ and $\sigma_{bC,t}$ as negligible relative to the variance from the denominator measurement error, which is captured by $\sigma_{C,t}^2$.

The expression simplifies to

$$\mathrm{Var}(\hat{a}_t) \approx \left(\frac{b_t}{C_t^2}\right)^2 \sigma_{C,t}^2.$$

Accordingly, a practical plug-in estimator is

$$\widehat{\mathrm{Var}}(\hat{a}_t) \approx \left(\frac{b_t}{\hat{C}_t^2}\right)^2 \widehat{\mathrm{Var}}(\hat{C}_t).$$

Data availability

The study uses publicly available Global Carbon Budget 2025 data and derived yearly series generated from those source files. The processed analysis tables are provided in the repository under the results directory, and the extracted and derived LULC panel is available as a CSV file in the data directory.

Code availability

All code used to process data, estimate models, and generate figures is available in the repository under the scripts directory, including Quarto analysis files and Julia helper functions.

Competing interests

The author declares no competing interests.

Additional information

Supplementary information is not included.